RAA 2020 Vol. **20** No. **1**, 8(12pp) doi: 10.1088/1674–4527/20/1/8

http://www.raa-journal.org *http://iopscience.iop.org/raa*

Research in Astronomy and Astrophysics

The subsurface structure and stratigraphy of the Chang'E-4 landing site: orbital evidence from small craters on the Von Kármán crater floor

Xiao-Hui Fu (付晓辉)[1,2], Le Qiao (乔乐)[1], Jiang Zhang (张江)[1], Zong-Cheng Ling (凌宗成)[1,3] and Bo Li (李勃)[1,4]

[1] Shandong Provincial Key Laboratory of Optical Astronomy and Solar-Terrestrial Environment, Institute of Space Sciences, Shandong University, Weihai 264209, China; *fuxh@sdu.edu.cn*

[2] State Key Laboratory of Lunar and Planetary Sciences, Macau University of Science and Technology, Taipa, Macau, China

[3] CAS Center for Excellence in Comparative Planetology, Hefei 230026, China

[4] State Key Laboratory of Remote Sensing Science, Institute of Remote Sensing and Digital Earth, Chinese Academy of Sciences, Beijing 100101, China

Received 2019 February 14; accepted 2019 August 2

Abstract Chang'E-4 (CE-4) successfully landed on the floor of the Von Kármán crater within the South Pole-Aitken basin (SPA). One of its scientific objectives is to determine the subsurface structure and the thickness of lunar regolith at the landing site and along the traverse route of the Yutu-2 rover. Using orbital data, we employed small craters (diameters <1 km) on the floor of the Von Kármán crater as probes to investigate the subsurface structure and stratigraphy of the CE-4 landing site. In this study, 40 dark-haloed craters that penetrate through the surface Finsen ejecta and excavate underlying mare deposits were identified, and 77 bright ray craters that expose only the underlying fresh materials but do not penetrate through the surface Finsen ejecta were found. The excavation depths of these craters and their distances from the Finsen crater center were calculated, and the thickness distribution of Finsen ejecta on the Von Kármán floor was systematically investigated. The boundary between Finsen ejecta and underlying mare basalt at the CE-4 landing site is constrained to a depth of 18 m. We have proposed the stratigraphy for the CE-4 site and interpreted the origins of different layers and the geological history of the Von Kármán crater. These results provide valuable geological background for interpreting data from the Lunar Penetrating Radar (LPR) and Visible and Near-infrared Imaging Spectrometer (VNIS) on the Yutu-2 rover. The CE-4 landing site could provide a reference point for crater ejecta distribution and mixing with local materials, to test and improve ejecta thickness models according to the *in situ* measurements of the CE-4 LPR.

Key words: Chang'E-4 — dark-haloed crater — ejecta thickness — Moon

1 INTRODUCTION

On 2019 January 3, Chang'E-4 (CE-4) safely landed in the eastern Von Kármán crater (186 km in diameter; central coordinates 44.4°S, 176.2°E) within the 2500-km-diameter South Pole-Aitken basin (SPA) (Li et al. 2019; Di et al. 2019). CE-4 is the first *in situ* exploration mission on the lunar farside as well as in the SPA basin. One scientific objective of this mission is to determine the mineral compositions of surface materials and perform geological characterization of the landing site (Jia et al. 2018). The Visible and Near-infrared Imaging Spectrometer (VNIS) and Lunar Penetrating Radar (LPR) aboard the Yutu-2 rover are the two key instruments for revealing the surface composition and subsurface structure of the landing site and the geological history of this region (Jia et al. 2018).

The Von Kármán crater is a perfect location to investigate both lunar farside volcanism and deep-seated materials possibly from the lunar upper mantle. The SPA is an ancient impact structure on the lunar farside (Wilhelms et al. 1979), which shows distinctive geochemical characteristics and has a unique geological history (e.g., Pieters et al. 1997; Lucey et al. 1998; Jolliff et al. 2000). Except for ultramafic mantle material exposure, previous studies also suggest the presence of differentiated impact melts at the bottom of the SPA basin (e.g., Morrison 1998; Hurwitz & Kring 2014; Vaughan & Head 2014). The Von Kármán crater lies within the Mg-pyroxene annulus defined by Moriarty III & Pieters (2018). Its floor was filled by mare basalts in the Late Imbrian Period (Pasckert et al. 2018). The basalt plains were subsequently reshaped by ejected materials from surrounding young craters. Both mare basalts and mafic materials with abundant Mg-rich pyroxene are exposed on the floor of the Von Kármán crater. The morphology, mineralogy, and geochemistry of Von Kármán crater were investigated (Huang et al. 2018; Ling et al. 2018, 2019; Qiao et al. 2019) using orbital data because it had been listed as the landing site of the CE-4 mission (Jia et al. 2018).

The subsurface structure of the CE-4 landing site contains a direct record of the sequence of major geological events and the geological history of this area. The impact structures in the regional vicinity of the Von Kármán crater span the vast expanse of geological time, from the pre-Nectarian SPA basin (Wilhelms et al. 1979) to the Nectarian Von Kármán crater (Stuart-Alexander 1978), the Imbrian Alder crater (82 km in diameter) (Wilhelms et al. 1987) and the Copernican Finsen crater (73 km in diameter) (Ling et al. 2019). Superpositions among these crater materials and mare basalt units establish local stratigraphic sequences. From lunar surface mineralogy and morphology analysis (Pasckert et al. 2018; Huang et al. 2018; Qiao et al. 2019), it has been widely accepted that the Finsen crater is the main source of surface ejecta in the eastern portion of the Von Kármán crater floor as well as at the CE-4 landing site (Pasckert et al. 2018; Li et al. 2019). However, several key questions about the subsurface structure and stratigraphy are still open. What is the thickness of Finsen ejecta? How much ejected material did these craters deliver to the Von Kármán crater floor? Is the Alder ejecta below or above the mare basalt unit? Stratigraphic investigations of the CE-4 landing site allow reconstruction of the general sequence of geological events in the region.

Small craters can penetrate through lunar surface geological units and act as probes into the underlying materials. Such craters have been widely used to determine the thickness of the surface unit and the compositions of lava flows, impact melt sheets beneath them and other hidden layers (Budney & Lucey 1998; Chen et al. 2018). Dozens of small craters (less than 2 km) are found on the floor of the Von Kármán crater. Based on these small crater studies, Huang et al. (2018) reported that the thickness of the 'fine grain' regolith varies from $\sim$2.5 to 7.5 m using the method of Quaide & Oberbeck (1968) in the landing region. In the present study, we attempt to use these craters to derive the thickness of Finsen ejecta and constrain the subsurface structure of the CE-4 landing site.

The small craters on the Von Kármán floor can be categorized into two distinct groups by the ejected material albedo around individual craters. One group is the craters surrounded by bright rays or ejecta patterns. These bright ray craters (BRCs) are relatively young. The bright continuous ejecta blanket is likely formed due to fresh material excavated by the primary crater. The other group comprises craters surrounded by low-albedo deposits known as dark-haloed craters (DHCs) (Head & Wilson 1979; Salisbury et al. 1968). The DHCs are interpreted as resulting from the excavation of low-albedo material from the subsurface, such mare basalts, glass materials or impact melts, although the nature and origin of DHCs are not completely understood (Head & Wilson 1979; Kaydash et al. 2014). The presence of DHCs has been taken as an indicator of ancient lunar volcanic deposits or cryptomaria (Bell & Hawke 1984; Whitten & Head 2015).

The crater excavation method can assess the thickness of Finsen ejecta and determine the vertical boundary between Finsen ejecta and mare basalts. On the Von Kármán floor, DHCs are craters that punch through overlying ejecta to excavate underlying mare material. BRCs expose only the underlying fresh materials but do not exhume the mare basalt layer below Finsen ejecta. Coordinated analyses of the crater excavation depths and their distances from the Finsen crater center can constrain the ejecta thickness.

To test this hypothesis, we searched the small craters in this area and identified the DHCs and BRCs. Their diameters (as well as estimated excavation depths) and distances from the Finsen crater were collected. Using these orbital datasets, we investigated the thickness and distribution of the Finsen ejecta on the Von Kármán floor. This study provides substantial geological background for CE-4 exploration, such as the stratigraphic sequences and major geological events in the SPA. The thickness estimates for different geological units at the CE-4 landing site are robust. Future measurements by the Yutu-2 rover will provide further insights into the subsurface setting of this area.

2 DATA AND METHODS

2.1 Data

We generated regional data mosaics of the Lunar Reconnaissance Orbiter (LRO) Wide-Angle Camera (LROC WAC, 100 m pixel^{-1}, Robinson et al. 2010), Narrow-Angle Camera (NAC, up to 0.60 m pixel^{-1}, Robinson et al. 2010), and Kaguya Terrain Camera (TC) Ortho mosaic (10 m pixel size; Haruyama et al. 2008) to perform the identification and topographic analysis of small craters on the Von Kármán floor. More details about WAC and NAC image processing are described in Qiao et al. (2019). LROC NAC images, with the highest spatial resolutions (0.5–2 m) of the lunar surface among all available orbital data, were acquired at different incidence angles. The NAC images covering the Von Kármán crater are all at moderate/high solar incidence angles ($>40°$).

The global mineral abundance maps (60 m pixel^{-1}) produced by Lemelin et al. (2016) from Kaguya MI spectrometer data were also used here. Quantitative mineralogical analysis for major rock-forming minerals (olivine, orthopyroxene, clinopyroxene and plagioclase) is obtained through radiative transfer modeling calculations. The Kaguya MI-extracted mineral abundance has a $1\sigma = 7$ wt% uncertainty from the Lunar Soil Characterization Consortium (LSCC) data (Lemelin et al. 2019). Kaguya MI-derived silicate abundance maps allow detailed mineralogical characterization of the Von Kármán floor and identification of small craters.

Identification of the DHCs and BRCs on the Von Kármán crater floor included three steps. First, the DHCs and BRCs were identified in the Kaguya TC mosaics, which provide nearly 100% coverage of the Von Kármán floor. Second, the DHCs and BRCs were confirmed on the NAC images with solar incidence angles less than 55°. In the third step, the identified DHCs and BRCs were rechecked on the Kaguya MI-extracted mineral abundance maps. DHCs on the Von Kármán floor should expose basaltic materials that are obviously different from the surrounding Finsen ejecta. The materials excavated by BRCs usually show mineral compositions similar to those of the surrounding terrain. This similarity occurs because these small craters do not penetrate the uppermost Finsen ejecta. Accurate measurements of small crater sizes were also performed based on Kaguya TC images and LROC NAC images.

In the present study, crater identification and diameter measurements were performed manually using the CraterTools extension in ArcMap (Kneissl et al. 2011). This tool has been extensively used in crater counting and diameter measurements in planetary science (e.g., Head et al. 2010). Crater diameter measurements are defined on the basis of a best-fit circle, fit to the crater rim based on three points selected along the rim. The center of this circle was taken as the crater position.

2.2 Ejecta Thickness Models and Crater Excavation Depth

The radial variations in Finsen ejecta thickness have also been estimated by ejecta thickness models. Based on observed ejecta thicknesses from explosion craters, terrestrial craters, and laboratory craters and on observations of ejecta from Copernicus and the Imbrium basin, several models have been developed to estimate the thickness of ejecta at a given distance from a crater. All these models are summarized in Table 1. In these equations, t is ejecta thickness, r is the distance from the center of the crater to a given location, and R_t is the radius of the transient crater. All these variables are in meters. For the present study, we utilized all these models to estimate the Finsen ejecta distributions on the Von Kármán crater floor. More details about these models are discussed in Section 4.

In the present study, the excavation depth ($H_{\rm exc}$) of each crater was calculated with the following equations in Melosh (1989): $H_{\rm exc} = 0.1D_t$, $D_t = 0.84D$, where D_t and D are the diameter of the transient crater and the final diameter, respectively. The final diameter of a small crater was obtained by the CraterTools extension in ArcMap. For the Finsen crater, the diameter (D) is 73 km, and R_t is 30.66 km.

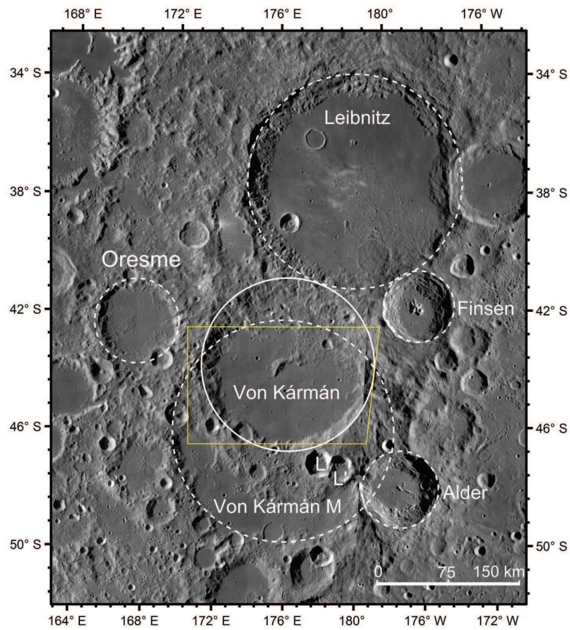

Fig. 1 LROC WAC image mosaic of the Von Kármán crater within the SPA basin. The *bold white circle* marks the rim location of the Von Kármán crater, and the *dotted white circles* mark the rim locations of the Von Kármán M, Leibnitz, Oresme and Finsen craters. The *yellow square* marks the position of Fig. 2. The projection is a Lambert conformal projection centered at 176°E, 44.5°S, and north is up.

2.3 Description of the Study Area

The Von Kármán crater is a Nectarian crater (Stuart-Alexander 1978) with degraded topographic and morphologic features (Fig. 1). This crater is surrounded by several other large impact craters: Leibnitz (~3.88 Ga, $D = 236$ km, Yingst et al. 2017) in the north, Finsen in the northeast, Von Kármán M ($D = 225$ km) /L/L′ in the south, Alder in the southeast, and Oresme (pre-Nectarian, $D = 73$ km, Wilhelms et al. 1979) in the west (Fig. 1). The Oresme crater, characterized by a damaged outer rim, is possibly older than the Von Kármán crater based on the geological map by Wilhelms et al. (1979). The Von Kármán M crater has been heavily destroyed by Von Kármán and thus relatively older. The ejecta of the Leibnitz crater buries the north rim crest of the Von Kármán crater, indicating its relatively young age. Clearly, Leibnitz and other young craters all delivered significant amounts of ejected materials onto the floor of the Von Kármán crater (Fig. 1).

The Finsen ejecta and mare basalts that filled in the Von Kármán crater exhibit different mineral and chemical compositions. The eastern portion of the Von Kármán

Table 1 Multiple Models to Estimate the Thickness of Ejecta

	Equations	References
1	$t = 0.14{R_t}^{0.74}(r/R_t)^{-3.0}$	McGetchin et al. (1973)
2	$t = 0.033R_t(r/R_t)^{-3.0}$	Pike (1974)
3	$t = 0.0078R_t(r/R_t)^{-2.61}$	Housen et al. (1983); Petro & Pieters (2008)
4	$t = 3.95(\pm1.19){R_t}^{0.399}(r/R_t)^{-3.0}$	Sharpton (2014)

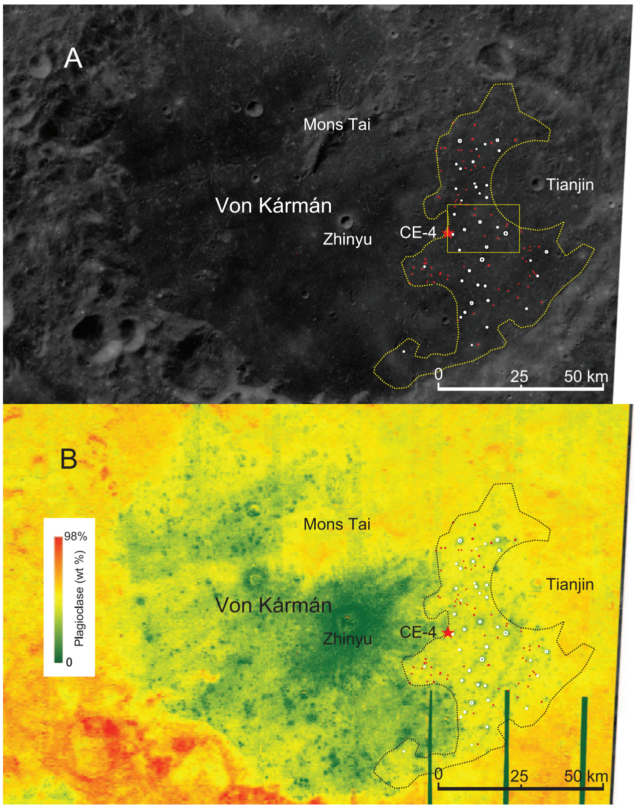

Fig. 2 Geological context of the study area and the identified small craters. Panel A is the Kaguya TC mosaic; Panel B shows the Kaguya MI-retrieved abundance mapping of plagioclase in the study area (Lemelin et al. 2016). The *dotted line* indicates the study area. The radial ejecta of the Zhinyu crater and the 15.2-km (4x its diameter) region around the Tianjin crater are excluded for the following small crater mapping to minimize the effects on the estimation of Finsen ejecta thickness. The *white* and *red circles* represent the DHCs and BRCs identified in the present study. The *yellow square* marks the position of Fig. 3. All the maps in this study are projected into the Lambert conformal 225 projection, centered at 176°E, 44.5°S, and north is up.

crater floor is homogeneous in surface FeO (11 wt%–13 wt%) and TiO_2 (1 wt%–2 wt%) content using Kaguya MI-derived elemental maps (Qiao et al. 2019). The mare deposits exposed by the Zhinyu crater show relatively elevated FeO abundances (13 wt%–18 wt%) and broader TiO_2 (1 wt%–3 wt%) range. Nearby mare materials show relatively higher average olivine (9 wt%±3 wt%) and clinopyroxene (16 wt%±4 wt%) abundances (Fig. 2). Finsen ejecta contain more feldspathic components, with an estimated average plagioclase abundance of 45 wt%±4 wt% (Qiao et al. 2019) (Fig. 2).

We define the study area for the small crater search using the Kaguya MI-derived plagioclase abundance map. Finsen ejecta are characterized by relatively elevated plagioclase abundance. On the plagioclase abundance map (Fig. 2B), Finsen ejecta shows a unique yellow tone. We define this area as the continuous ejecta blanket of the Finsen crater (dotted line polygon in Fig. 2). The boundary between the Von Kármán crater floor and wall is adapted from the mare boundary defined by Nelson et al. (2014). The CE-4 landing site (red star in Fig. 2) is located on the western edge of the study area.

At the edges of the study area, we observe two craters with diameters >3.5 km (Fig. 2). The Zhinyu crater (3.6 km in diameter) is fresh and has a sharp and raised rim. The Tianjin crater (3.6 km in diameter) lies at the base of the Von Kármán inner wall and is moderately degraded. On the plagioclase abundance map, the Zhinyu crater produces radial mare deposits with lower plagioclase and delivers them to the adjacent regions. The regions that may contain ejecta derived from this crater are all excluded here. The Tianjin crater does not show an obvious compositional contrast with the surrounding terrain. Nevertheless, any craters within the 15.2-km region (4 times its diameter) around the Tianjin crater are ruled out for the small crater search.

3 RESULTS

3.1 The Identification of Dark-haloed Craters

Dark-haloed craters were identified in the study area following the three steps in Section 2.1. The DHC candidates firstly identified on the Kaguya TC images were then reexamined on the NAC images (see examples in Fig. 3). Previous studies proposed that the solar incidence angles can affect small craters' detection and measurement (Ostrach et al. 2011; Antonenko et al. 2013). To examine this, we compared numerous NAC images of the same area taken with different incidence angles. Small craters and their surrounding ejecta show significant albedo variations and no shadows in the NAC images with low incidence angles. The images with incidence angles of less than 20° are the ideal NAC dataset for a small crater search. However, the NAC images that cover the study area were all acquired at incidence angles larger than 40°. Therefore, the NAC images with incidence angles of $40° - 55°$ were used for small craters' identification and validation. Due to the incomplete coverage of the NAC images with incidence angles $40° - 55°$ in the study area, some BRC candidates cannot be verified. These craters were not involved in the following ejecta estimation.

The abundance maps of silicates obtained by Kaguya MI (Lemelin et al. 2016) were also applied for verification of DHCs. As mentioned above, mare basalts are characterized by a lower abundance of plagioclase (Pl) and higher abundances of olivine (Ol) and clinopyroxene (CPX) than Finsen ejecta. On the P1 abundance map, we can easily recognize the isolated green spots on the yellow-toned Finsen ejecta (Figs. 2B and 4C). The green spots, consisting of green-toned ejecta from the Zhinyu crater, represent mare materials from the mare basalt layer beneath Finsen ejecta. Therefore, Pl abundance variations between exhumed mare deposits and Finsen ejecta distinguish them and enable us to check the DHCs. Figure 4 shows eight typical DHCs found near the CE-4 landing site. On the abundance maps of Pl, Ol and CPX (Figs. 4B–D), we note that the locations and sizes of the DHCs measured in the Kaguya TC and LROC NAC images match well with the crater shapes outlined by mineral distributions. All the DHCs identified on Kaguya TC and LROC NAC images are confirmed in the abundance maps of silicates.

3.2 The Identification of Bright Ray Craters

Bright ray craters are characterized by high-albedo deposits occurring around the crater (Hawke et al. 2004). Most small craters with typical bright rays can be identified in Kaguya TC images. However, due to the low spatial resolution of Kaguya TC images, it is difficult to accurately measure the diameters of these craters. The high spatial resolution images acquired by the LROC NAC were used. In the NAC images with incidence angles of $40° - 55°$, fresh ejecta of these craters show enhanced contrast with the background, which makes BRCs easily recognizable (Fig. 3). We identified 77 BRCs and determined their diameters and center locations on the NAC images. On Kaguya MI-retrieved abundance maps of silicates, these craters usually show no obvious compositional contrast with the surrounding terrain, indicating that they did not penetrate through the Finsen ejecta (Fig. 4).

3.3 Crater Excavation Depth and Ejecta Thickness

We estimated the thickness of Finsen ejecta on the floor of the Von Kármán crater using the small craters that completely penetrated (DHCs) and failed to penetrate (BRCs) through this ejecta layer. In the study area, 40 DHCs and 77 BRCs were identified. Their diameters, crater centers, distances from the Finsen crater center, and estimated excavation depths are listed in Tables 2 and 3. The excavation depth of each crater was estimated using the crater excavation equation of Melosh (1989) (see the equation in sect. 2.2). All of the craters are simple impact structures with bowl-shaped interiors and smooth walls (see the examples in Fig. 3). Their distances from the center of the Finsen crater vary from 110 to 180 km. Most of the DHCs range from 400 to 800 m in diameter (Fig. 5). The BRCs are relatively small, with diameters of less than 250 m (Fig. 5).

Figure 6 shows the correlation of crater excavation depths with their distances from the Finsen crater center. Note that the DHCs (red circles) and BRCs (green diamonds) are clearly plotted in two clusters. An obvious boundary is found between these clusters. The DHCs are concentrated above this boundary, while the BRCs are located below the boundary. This result is reasonable because the DHCs have larger diameters and excavation depths than the BRCs. The boundary between the 'penetrating' DHCs and the 'non-penetrating' BRCs (Fig. 6) approaches the true thickness of Finsen ejecta distributed on the eastern portion of the Von Kármán crater floor.

Finsen ejecta thickness was also estimated using ejecta thickness models (Table 1). The Finsen ejecta distributions derived from these models follow the same trend (Fig. 6): the ejecta thickness decays exponentially with the radial distance. However, the curves built based on these models are all lower than the boundary constrained by small craters (Fig. 6). This result suggests that all these model-

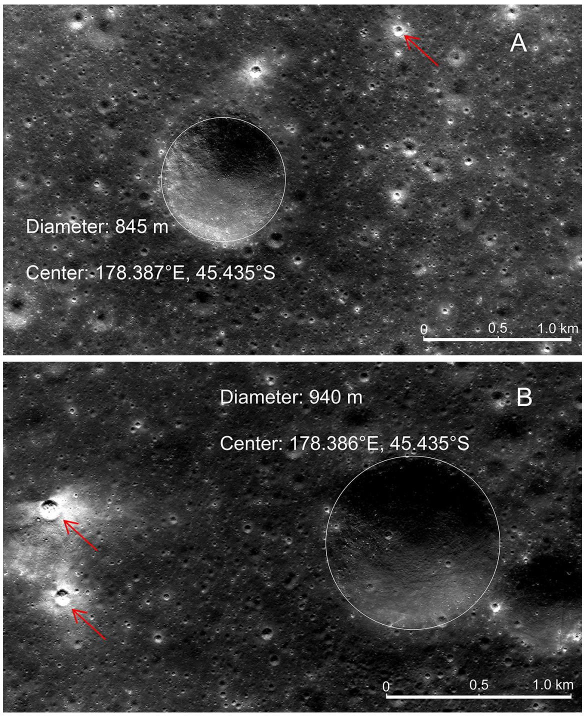

Fig. 3 Typical DHCs and BRCs on the eastern floor of the Von Kármán crater. *White circles* represent the best-fit circles of two DHC rims. BRCs with high-albedo rays are also noted (*red arrows*). The NAC image IDs are M141099568R and M1148327111L.

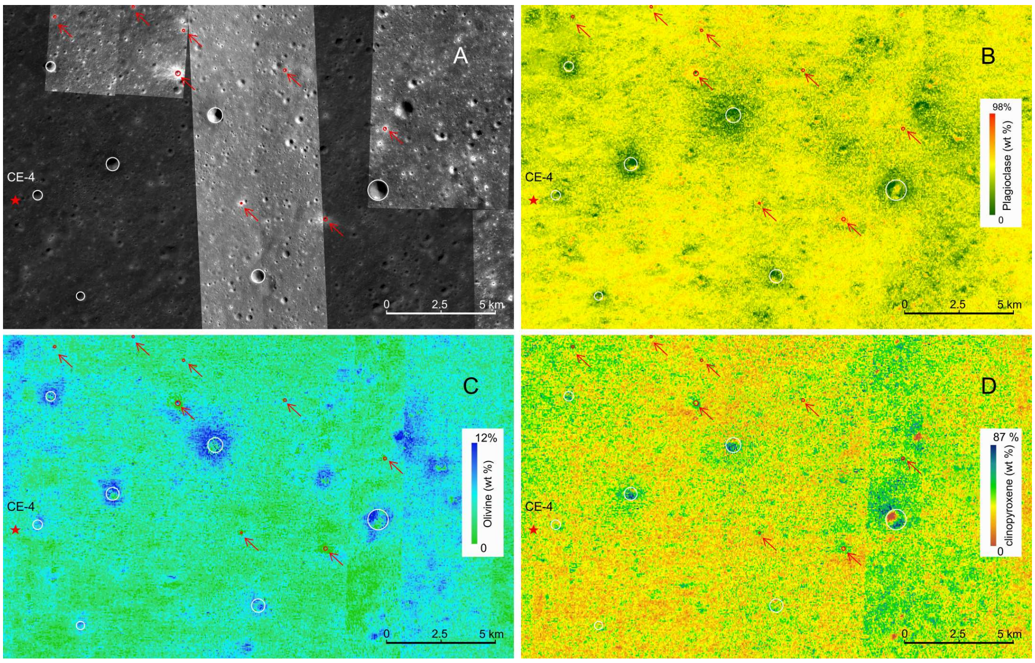

Fig. 4 DHCs and BRCs identified on the orbital images and Kaguya MI-retrieved abundance maps of silicates. Panel A presents LROC NAC images overlaid on the Kaguya TC mosaic. The IDs of the NAC images used here for small crater identifications are M1145979809L, M1145979809R, M143453659L, M143453659R, M1229577647L, and M1229577647R. Panels B, C, and D are Kaguya MI-retrieved abundance maps of plagioclase, olivine, and clinopyroxene, respectively. The *white* and *red circles* in the 4 panels represent the best-fit circles of DHCs and BRCs, respectively. DHCs exhume basaltic materials with lower Pl and higher Ol and CPX contents. *Red arrows* indicate the identified BRCs, which show no compositional contrast with the background. The *red star* shows the location of the CE-4 landing site.

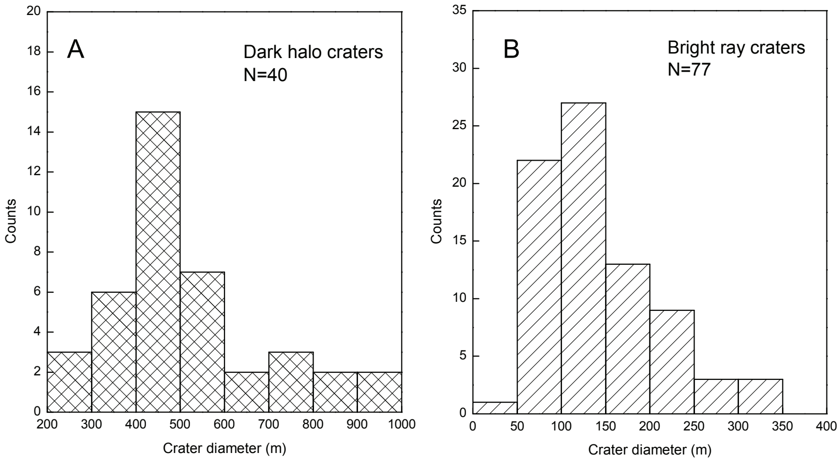

Fig. 5 Histogram of diameters for DHCs (A) and BRCs (B) identified in the study area.

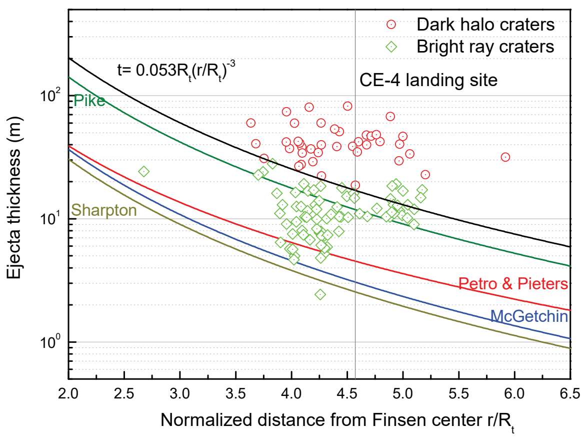

Fig. 6 Thickness estimates for the Finsen ejecta plotted as a function of the distance from Finsen center. The *red circles* and *green diamonds* represent the DHCs and BRCs identified in the study area. Their distance from Finsen crater center (Tables 2 and 3) have been normalized to the transient radius of Finsen crater ($R_t = 30.66$ km). The *solid curves* present the thickness of Finsen ejecta calculated using the different models (see equations in Table 1). The *vertical gray line* represents the CE-4 landing site ($r = 140.15$ km, $r/R_t = 4.57$). Its distance from the Finsen crater center ($r = 140.15$ km) is calculated based on the landing location (177.588° E, 45.457° S) reported by Di et al. (2019).

s might underestimate the thickness of the Finsen ejecta. Among the five models, the curve built based on the equation of Pike (1974) is closest to the boundary in Figure 6. We followed the approach of Pike (1974) and revised their equation as $t = 0.053R_t(r/R_t)^{-3.0}$. This revised equation (black curve in Fig. 6) gives the best fit to the actual ejecta thickness in the normalized distance range 3.5–4.7. In Section 4.1, we discuss possible reasons for the deviations of these ejecta thickness models.

4 DISCUSSION

4.1 Possible Reasons for the Underestimation of Ejecta Thickness Models

Several ejecta thickness models have been proposed to estimate the ejecta thickness and spatial distribution around a crater. The ejecta thickness can be expressed as a function of the crater size and the distance between the crater center and a location of interest. It is generally described as $t = T(r/R_t)^b$, where t is the thickness at radial distance r from the crater center, T is the ejecta thickness at the rim of the crater, R_t is the radius of the transient crater, and b is the exponent of the power law.

The models of McGetchin et al. (1973) and Pike (1974) are the most cited models for eject thickness estimation (e.g., Xie & Zhu 2016; Zhu et al. 2015). McGetchin et al. (1973) developed a power law equation based on the results of nuclear and high explosive cratering events, small-scale laboratory cratering experiments, natural meteorite impact craters, and estimates for lunar craters, including numerous cratering events. They defined T and b as $T = 0.14{R_t}^{0.74}$, $b = -3$. Pike (1974) modified this equation in consideration of the thickness of ejecta at the rim of terrestrial analogs and experimental explosion craters. Pike (1974) revised the equation for T: $T = 0.033R_t$. Generally, the Pike equation predicts approximately an order of magnitude greater amount of material introduced to any given location on the surface than the McGetchin model.

Housen et al. (1983) developed another model based on dimension analysis of impact cratering. This model is applicable to different planetary surfaces and contains several variables depending on the target properties. Petro & Pieters (2004) simplified the Housen et al. (1983) scaling equation and suggested $T = 0.0078R_t$, $b = -2.61$. Sharpton (2014) investigated lunar craters with diameters

Table 2 DHCs Identified in the Study Area

Crater diameter (km)	Lon (°)	Lat (°)	Distance from Finsen center (km)	Excavation depth (m)	Crater diameter (km)	Lon (°)	Lat (°)	Distance from Finsen center (km)	Excavation depth (m)
0.607	177.80	–45.41	135.82	51.03	0.410	177.67	–45.00	129.99	34.48
0.712	178.01	–45.33	130.78	59.78	0.489	177.95	–44.98	124.90	41.08
0.958	178.38	–45.43	127.54	80.47	0.460	177.65	–45.26	135.12	38.63
0.709	178.97	–45.60	123.50	59.57	0.407	177.67	–44.76	125.64	34.16
0.636	178.12	–45.57	134.51	53.46	0.502	177.73	–45.61	141.06	42.13
0.975	178.06	–45.70	138.10	81.93	0.400	177.77	–46.28	155.19	33.62
0.569	177.88	–45.81	143.23	47.77	0.376	176.87	–46.88	181.47	31.56
0.503	177.77	–45.91	147.01	42.23	0.461	177.63	–45.46	139.43	38.75
0.558	178.01	–45.95	144.55	46.84	0.506	178.10	–45.08	124.47	42.53
0.473	178.11	–45.96	143.30	39.77	0.328	178.00	–45.04	125.33	27.58
0.555	177.83	–46.23	153.26	46.59	0.442	178.09	–44.96	122.11	37.13
0.805	177.92	-46.13	149.85	67.58	0.318	177.92	-44.95	124.69	26.71
0.574	178.16	–46.10	145.99	48.19	0.222	177.96	–45.73	140.24	18.68
0.713	178.23	–44.51	111.50	59.88	0.415	178.71	–46.17	140.73	34.84
0.880	177.69	–44.53	121.30	73.89	0.480	178.15	–46.37	152.41	40.34
0.454	177.72	–44.80	125.51	38.17	0.484	178.26	–44.61	112.85	40.61
0.439	178.26	–45.37	128.00	36.84	0.352	177.24	–45.78	152.20	29.57
0.368	178.07	–44.55	115.09	30.90	0.272	177.94	–46.55	159.44	22.83
0.473	178.85	–45.84	130.85	39.76	0.500	177.90	–44.73	121.20	41.98
0.346	178.75	–45.69	128.54	29.07	0.265	177.75	–45.12	130.91	22.22

from 2.2 to 45 km. They followed the model of McGetchin et al. (1973) and proposed that the ejecta thickness at the rim of a complex crater is $T = 3.95(\pm1.19)R_t{}^{0.399}$.

The underestimation of these models, relative to the ejecta thicknesses indicated by the DHCs and BRCs identified in this study, may be related to their assumptions and limitations. The McGetchin model was noted to have been established from inadequate lunar data and to be inconsistent with the general form of either empirical or theoretical studies of craters (Pike 1974; Xie & Zhu 2016). The Housen et al. (1983) model was corrected to account for the curvature of the Moon (Petro & Pieters 2004) to investigate the mixing of materials excavated by impact basins on a global scale. This is clearly not the case for the Finsen ejecta distribution on the Von Kármán crater floor. The Sharpton (2014) model was based on investigations of 21 small-scale impact craters on the Moon. This equation should not be extrapolated to large complex craters such as the Finsen crater (73 km in diameter, with a central peak) because the formation conditions (such as the size of projectiles and transient cavity diameter; Xie & Zhu 2016) of the Finsen crater were different from those of craters with diameters of 2–45 km.

The underestimation of the ejecta models may be due to the contribution of other craters in addition to Finsen. Based on the surface morphology and mineralogical features of the study area, the Finsen crater is the main source of the surface ejecta layer. However, other craters, older than Finsen but younger than Von Kármán volcanism, might also have contributed. Such an ejecta layer should lie between the surface Finsen materials and the mare basalts. The Alder crater is one candidate to have transported ejected materials to the study area (Fig. 1). Alder is an Imbrian crater that is clearly older than Finsen crater. However, the sequence of the Alder impact event and the Von Kármán volcanism is quite ambiguous. In the western portion of Von Kármán, Finsen ejecta becomes thin to discontinuous with increasing distance from the Finsen center. If Alder ejecta lies on mare basalt units, there should be unique morphological features for tracking their source region, such as linear features and secondary impact craters/crater-chains. However, we found no morphological evidence in the western portion of the Von Kármán floor. This observation indicates that the materials in the western portion of the Von Kármán floor should not have been derived from the Alder crater. We suggest that the formation of the Alder crater should have been earlier than the emplacement of mare basalt; thus, Alder ejecta could lie beneath the basalt layer. There are two craters on the rim of the Von Kármán crater: Von Kármán L (Eratosthenian, $D = 29$ km) and L′ (Imbrian, $D = 29$ km). Their contributions can also be ignored because of their young ages and relatively small sizes. In summary, the superposition relationships rule out the possible contribution of ejecta materials from other craters.

4.2 The Stratigraphy of the CE-4 Landing Site

The SPA is the largest and oldest recognizable impact basin on the Moon. It is a high-priority landing site for scientific

Table 3 BRCs Identified in the Study Area

Crater diameter (km)	Lon (°)	Lat (°)	Distance from Finsen center (km)	Excavation depth (m)	Crater diameter (km)	Lon (°)	Lat (°)	Distance from Finsen center (km)	Excavation depth (m)
0.219	177.94	–45.26	130.68	18.41	0.200	177.44	–44.60	127.14	16.81
0.155	177.95	–45.20	129.18	13.01	0.229	177.50	–44.60	126.03	19.23
0.092	177.83	–45.16	130.29	7.72	0.333	177.89	–44.50	117.44	28.00
0.029	177.80	–45.15	130.56	2.43	0.286	177.91	–44.37	114.79	24.00
0.086	177.73	–45.14	131.61	7.26	0.121	177.30	–45.93	154.48	10.17
0.062	177.74	–45.15	131.66	5.20	0.288	178.47	–44.40	82.06	24.21
0.070	177.67	–45.13	132.45	5.91	0.205	177.05	–45.95	158.56	17.19
0.069	177.69	–45.11	131.75	5.80	0.177	178.03	–46.54	158.14	14.86
0.092	177.70	–45.06	130.59	7.72	0.145	178.23	–46.15	146.08	12.16
0.080	177.82	–45.01	127.69	6.76	0.192	177.99	–44.67	118.62	16.13
0.094	177.45	–44.83	130.71	7.90	0.124	177.80	–45.77	143.49	10.43
0.123	177.57	–45.90	149.69	10.35	0.192	178.58	–46.07	139.68	16.13
0.124	177.59	–45.87	148.72	10.41	0.176	178.44	–46.00	139.90	14.76
0.138	177.35	–45.87	152.32	11.62	0.059	177.76	–44.73	123.49	4.98
0.173	177.48	–45.84	149.81	14.52	0.090	177.69	–44.62	122.96	7.54
0.155	177.35	–45.79	150.65	13.01	0.068	177.73	–44.62	122.16	5.69
0.127	177.22	–45.81	153.05	10.65	0.108	177.93	–44.77	121.28	9.08
0.107	177.08	–45.86	156.31	8.99	0.150	177.80	–44.80	124.04	12.57
0.155	177.10	–45.79	154.60	13.00	0.067	177.88	–44.81	122.92	5.65
0.228	177.25	–45.75	151.37	19.15	0.132	178.05	–44.78	119.44	11.07
0.132	177.28	–45.74	150.82	11.05	0.142	177.74	–46.31	156.34	11.94
0.220	177.27	–45.71	150.30	18.51	0.129	177.66	–45.18	133.50	10.86
0.212	178.92	–46.10	136.45	17.83	0.076	177.88	–44.63	119.59	6.42
0.119	178.74	–45.85	132.34	10.04	0.270	178.14	–44.54	113.50	22.71
0.123	178.59	–45.93	136.26	10.37	0.149	178.72	–45.95	135.18	12.51
0.087	178.83	–45.83	130.87	7.27	0.200	177.38	–45.93	153.29	16.81
0.057	178.79	–45.80	130.64	4.81	0.153	177.96	–46.24	151.80	12.83
0.073	178.80	–45.82	130.76	6.11	0.131	178.30	–45.99	141.32	11.01
0.099	178.68	–45.70	129.59	8.30	0.123	178.17	–45.25	126.81	10.30
0.118	178.63	–45.67	129.59	9.90	0.150	178.40	–45.34	125.27	12.57
0.194	178.86	–45.55	123.72	16.33	0.155	177.61	–44.35	120.15	13.00
0.096	178.73	–45.56	125.53	8.04	0.204	177.38	–44.63	128.78	17.09
0.138	178.65	–45.57	127.02	11.62	0.055	178.59	–45.38	123.32	4.66
0.124	178.73	–45.59	126.36	10.41	0.112	178.60	–45.41	123.95	9.43
0.167	178.27	–45.48	130.24	14.04	0.088	178.39	–45.36	125.92	7.40
0.124	177.42	–45.08	135.78	10.40	0.135	177.47	–45.86	150.20	11.33
0.094	177.44	–45.10	135.63	7.90	0.088	178.08	–45.46	132.57	7.38
0.123	178.15	–45.76	138.20	10.30	0.142	177.41	–44.71	129.54	11.95
0.181	178.16	–45.75	137.84	15.22					

human and robotic exploration missions (e.g., Jolliff et al. 2012). The nature and formation of the SPA basin have implications for several fundamental questions about lunar early evolution (Jolliff et al. 2017; Shearer et al. 2011) including lunar impact chronology, large impact basin formation, and lunar farside volcanism. Lunar stratigraphy is significant for understanding the geological history and geological event sequence of the study area (Fig. 1). The Von Kármán crater is located on the impact breccia/melt sheet produced by the SPA impact event. After the formation of the Von Kármán crater (Nectarian Period), its floor was resurfaced by multiple ejecta blankets from the surrounding craters and filled with low-Ti mare basalts. In this section, we investigate the superposition of materials on the floor of the Von Kármán crater and construct the stratigraphy of the study area as well as of the CE-4 landing site.

Finsen ejecta composes the uppermost layer in the study area (Fig. 7). Finsen ejecta, the yellow tones in the Pl abundance map (Fig. 2B), widely covers the study area. These OPX-rich (and CPX-poor) materials may have originated from the lunar mantle (Li et al. 2019), which will be continuously investigated by the Yutu-2 rover. According to the mineralogical characterization of materials exhumed by craters, low-Ti mare basalt represents the layer below the Finsen ejecta. The low-Ti basalt emplacement in the Von Kármán crater occurred at 3.6 Ga (Huang et al. 2018). This basalt layer was finally covered by Finsen ejecta at 969 ± 130 Ma (Ling et al. 2019). Based on the DHC and BRC excavation depth calculations, we conclude that the vertical depth of the boundary between the overlying ejecta layer and the mare basalt layer is approximately 18 m at the CE-4 landing site.

Both the Finsen ejecta and mare basalt layers have long exposure histories on the lunar surface. Regolith layers should have developed on the top surfaces as a result of long-continued bombardment. We propose that, prior to the superposition of the Finsen ejecta, a basaltic regolith layer developed on the surface of the mare basalt plains. The surface of the mare deposits was affected by subsequent impact events since their emplacement at 3.6 Ga and was gradually reworked by micrometeorites and solar wind ions until the surface was finally buried by Finsen ejecta at 969±130 Ma (Ling et al. 2019). We estimated that the thickness of the ancient basaltic regolith layer is approximately 4–5 m, the same as the average regolith thickness in lunar mare regions (McKay et al. 1991). The ancient basaltic regolith layer was very likely disturbed by the impact transport of Finsen ejecta and mixed with these foreign materials. This mixing occurred because the material in the primary ejecta curtain interacted with and incorporated local material (Oberbeck 1975). Thus, there should have developed a transitional and mixed zone near the boundary between Finsen ejecta and mare basalt (shaded regions in Fig. 7). However, it is difficult to assess the thickness of the mixed zone.

The Finsen ejecta has also been continually reworked by small young craters since ejecta formation. We suggest that a regolith layer exists on the top surface of the Finsen ejecta. The regolith layer should be a fine-grained, homogeneous mixture of local materials, compared with the underlying rocks. Huang et al. (2018) assessed the regolith thickness in a rectangular area (average 5.8 km in the E-W direction and 2.4 km in the N-S direction, including the CE-4 landing site) using NAC images with incidence angles of less than 55°. They estimated that the regolith thickness in this area varies from ∼2.5 to 7.5 m. It is not possible to estimate the regolith thickness at the CE-4 landing site using the same method because the CE-4 site is not covered by these NAC images with incidence angles of less than 55°. However, the rectangular area in the eastern portion of the Von Kármán crater is a relatively small and smooth plain, which clearly has the same exposure history and impact flux. Therefore, we assume that the local regolith layer of the CE-4 landing site has the same thickness as the rectangular area of Huang et al. (2018).

To reveal the deeper layers, relatively large craters on the floor of the Von Kármán crater are needed. The largest crater near the study area is the Zhinyu crater. It is approximately 3.6 km in diameter with an estimated excavation depth of 310 m. This crater exposed massive mare deposits (Fig. 2B), indicating that it did not penetrate through the mare basalt layer. The bottom of the mare basalt layer must be deeper than 310 m. There are no craters on the Von Kármán floor that exhume materials beneath the mare basalts. Therefore, the crater excavation method cannot provide further stratigraphic information at greater depths.

The superposed relationships of these ‘hidden’ layers under the mare basalt layer have been interpreted according to the ages of the craters (Huang et al. 2018). The Nectarian Leibnitz crater and Imbrian Alder crater both delivered ejecta to the Von Kármán floor. The CE-landing site is 224 and 134 km from the Leibnitz and Alder crater centers, respectively. Using the proposed model (the equation in Fig. 6), we estimate that the thicknesses of Leibnitz and Alder ejecta at the CE-4 landing site are approximately 520 and 29 m, respectively. The materials below Leibnitz ejecta should be impact breccias/melts, which usually occur on the fractured floor of a crater according to terrestrial impact structure studies. We assume that the SPA basin is the oldest lunar basin; thus, its impact breccia/melts form the base of the stratigraphy of the study area.

The stratigraphy of the CE-4 landing site is determined based on the results of small crater mapping and geological investigations of the study area (Fig. 7). A brief geological history of the study area is proposed as follows: A Nectarian impact event formed the Von Kármán crater with a central peak, and impact melts/breccia spread on the crater floor; the Leibnitz impact event produced mass materials that overlaid the northern rim and floor of the Von Kármán crater; the formation of the Alder crater also transported a thin layer of exhumed materials; basaltic volcanism was active at 3.6 Ga, and low-Ti basalt flows filled most of the floor; a basaltic regolith layer formed on the surface of the mare basalt plain; in the long Eratosthenian Period, no large crater formed in the adjacent area, and basaltic regolith formed on the surface of the mare basalt; the Copernican Finsen impact ejecta overlaid the basalt unit and covered the study area; subsequent small impact events struck the surface, and some of them excavated the underlying basaltic materials and formed the craters with dark halos.

4.3 Implications for the CE-4 Mission

The LPR aboard the Yutu-2 rover is planned to determine the subsurface structure and the depth of the subsurface layers. It covers two channels with different penetration depths: a low-frequency channel (CH-1, 60 MHz) and a high-frequency channel (CH-2, 500 MHz) (Guo et al. 2019; Jia et al. 2018). CH-1 is designed to determine the subsurface structure to a depth of several hundreds of meters. CH-2 is intended to detect the fine structure of the lunar regolith with a penetration depth of ∼10 m (Guo et al. 2019; Jia et al. 2018).

The results of LPR CH-1 can refine the established stratigraphic column and answer several key questions about deep layers at the CE-4 landing site. These results will reveal more structural details, such as the mixed zone between Finsen ejecta and mare basalt, the thicknesses of Finsen ejecta and basaltic regolith, and the superposition relationship of Alder ejecta and mare deposits. LPR will also yield the thicknesses of mare basalts and possible sublayers, which will provide significant information for understanding lunar volcanism and assessing the volume of mare deposits. LPR CH-2 will reveal the fine subsurface structure of the regolith layer in meters, comparable with the Apollo drill cores. The CE-4 landing site shows the superposition of multiple ejecta layers. The *in situ* measurements of LPR could serve as reference points to investigate

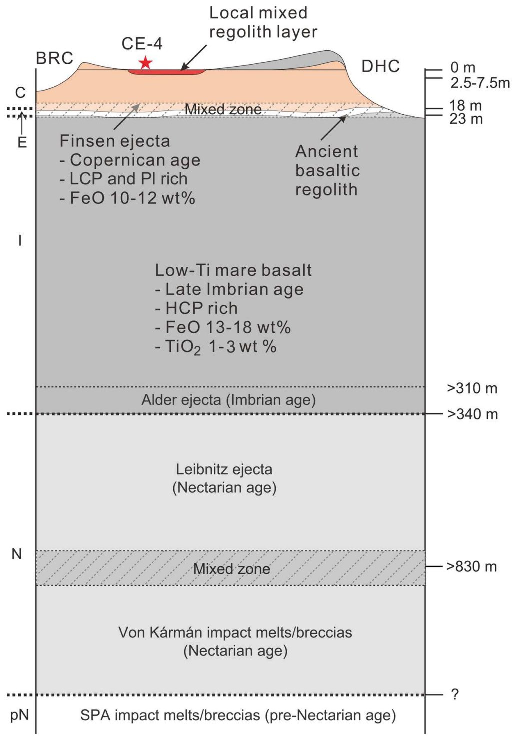

Fig. 7 The stratigraphy and subsurface structure proposed in the present study. The depth and layer thickness are not scaled in this profile. The *red star* indicates the CE-4 landing site. Typical DHCs and BRCs are shown here. The chemical and mineralogical compositions of Finsen ejecta and mare basalts are from Qiao et al. (2019) and Ling et al. (2019). The *shaded regions* indicate the mixed zone between the impact ejecta and the underlying layer. The *letters* on the left represent lunar geological periods: pN for pre-Nectarian, N for Nectarian, I for Imbrian, E for Eratosthenian, and C for Copernican.

the ejecta thickness and mixing effects with local materials. The above ejecta thickness models could be tested and improved according to the *in situ* observations of the CE-4 LPR.

The *in situ* investigation of VNIS onboard the Yutu-2 rover has identified olivine and low-Ca pyroxene in the soil at the CE-4 landing site (Li et al. 2019). These materials have been interpreted as the ejecta from the Finsen crater, which may represent deep-seated materials emplaced at the time that the SPA basin formed (Li et al. 2019). Kaguya MI data agree with the spectral observations by the Yutu-2 rover on the presence of OL and OPX in the Finsen ejecta. However, the abundant plagioclase (average 45%$\pm$4 wt%) components derived from the Kaguya MI data indicate these materials are more likely to originate from the differentiated melt sheet at the base of the SPA basin (e.g., Morrison 1998; Hurwitz & Kring 2014; Vaughan & Head 2014). Continued exploration by the Yutu-2 rover will target various surface materials on the eastern floor of the Von Kármán crater and reveal their geological implications for understanding the evolution of the SPA. Using the orbital dataset, this study identified the craters that may have delivered materials to the CE-4 landing site and specifies their ejecta thicknesses and superposition relationships. This information will contribute to the CE-4 mission and help us understand the geological context and the origin of various materials.

5 CONCLUSIONS

We identified 40 dark-haloed craters on the Von Kármán crater floor that have penetrated through the surface Finsen ejecta and excavated underlying mare deposits and 77 bright ray craters that expose only the underlying fresh materials. Based on the small cater mapping, we constrained the Finsen ejecta thickness at the CE-4 landing site. We have provided a proposed stratigraphy for the CE-4 site and interpreted the origins of different layers and the geological history of the Von Kármán crater. These results provide valuable geological background for interpreting data from LPR and VNIS on the Yutu-2 rover. We suggest that the CE-4 landing site could serve as a reference point for crater ejecta distributions and mixing effects with local materials, which could be used to test and improve ejecta thickness models according to the results of the CE-4 LPR.

Acknowledgements The authors thank Professor Meng-Hua Zhu, Professor Feng Zhang, and Dr. Ming-Gang Xie for their helpful discussions. We gratefully acknowledge very constructive and helpful reviews provided by Dr. Joshua Snape and an anonymous reviewer that significantly improved the original version of the manuscript.

Fu, X. H., was supported by the National Natural Science Foundation of China (Grant Nos. 41490633 and 41590851), the open fund of the State Key Laboratory of Lunar and Planetary Sciences (Macau University of Science and Technology) (Macau FDCT Grant No. 119/2017/A3), and the open fund of the Key Laboratory of Lunar and Deep Space Exploration, Chinese Academy of Sciences. Ling, Z. C., was supported by the National Natural Science Foundation of China (U1931211, 41972322 and 11941001), the Natural Science Foundation of Shandong Province (ZR2019MD008), and Qilu (Tang) Young Scholars Program of Shandong University, Weihai (2015WHWLJH14). Li, B., was supported by the Program for JLU Science and Technology Innovative Research Team (JLUSTIRT, 2017TD-26), the Focus on Research and Development Plan in Shandong Province (2018GGX101028), and the Shandong Provincial Natural Science Foundation (ZR2019MD015).

All original LROC images are available at NASA's Planetary Data System (`http://pds.nasa.gov/`), Kaguya TC images are archived at the SELENE Data Archive (`https://darts.isas.jaxa.jp/planet/pdap/selene/`), and Kaguya MI mineral maps are available at the Imaging Annex of the Planetary

Data System (`http://astrogeology.usgs.gov/pds/annex`).

References

Antonenko, I., Robbins, S. J., Gay, P. L., Lehan, C., & Moore, J. 2013, in Lunar and Planetary Science Conference, 44, 2705

Bell, J. F., & Hawke, B. R. 1984, Journal of Geophysical Research: Planets, 89, 6899

Budney, C. J., & Lucey, P. G. 1998, Journal of Geophysical Research: Planets, 103, 16855

Chen, Y., Li, C., Ren, X., et al. 2018, Journal of Geophysical Research: Planets, 123, 630

Di, K., Liu, Z., Liu, B., et al. 2019, Journal of Remote Sensing, 23, 177

Guo, D., Fa, W., Zeng, X., et al. 2019, in Lunar and Planetary Science Conference, `https://www.hou.usra.edu/meetings/lpsc2019/pdf/1844.pdf`

Haruyama, J., Matsunaga, T., Ohtake, M., et al. 2008, Earth, Planets and Space, 60, 243

Hawke, B., Blewett, D., Lucey, P., et al. 2004, Icarus, 170, 1

Head, J. W., Fassett, C. I., Kadish, S. J., et al. 2010, Science, 329, 1504

Head, J. W., & Wilson, L. 1979, in Lunar and Planetary Science Conference, 10, 2861

Housen, K. R., Schmidt, R. M., & Holsapple, K. A. 1983, Journal of Geophysical Research: Planets, 88, 2485

Huang, J., Xiao, Z., Flahaut, J., et al. 2018, Journal of Geophysical Research: Planets, 123, `https://doi.org/10.1029/2018JE005577`

Hurwitz, D. M., & Kring, D. A. 2014, Journal of Geophysical Research: Planets, 119, 1110

Jia, Y., Zou, Y., Ping, J., et al. 2018, Planetary and Space Science, 162, 207

Jolliff, B. L., Gillis, J. J., Haskin, L. A., Korotev, R. L., & Wieczorek, M. A. 2000, Journal of Geophysical Research: Planets, 105, 4197

Jolliff, B. L., Shearer, C. K., & Cohen, B. A. 2012, in Annual Meeting of the Lunar Exploration Analysis Group, 1685, 3047

Jolliff, B. L., Shearer, C. K., Papanastassiou, D. A., Liu, Y., & Team, M. S. 2017, in Lunar and Planetary Science Conference, 48, 1300

Kaydash, V., Shkuratov, Y., & Videen, G. 2014, Icarus, 231, 22

Kneissl, T., van Gasselt, S., & Neukum, G. 2011, Planetary and Space Science, 59, 1243

Lemelin, M., Lucey, P. G., Gaddis, L. R., Hare, T., & Ohtake, M. 2016, in Lunar and Planetary Science Conference, 47, 2994

Lemelin, M., Lucey, P. G., Miljkovic, K., et al. 2019, Planetary and Space Science, 165, 230

Li, C., Liu, D., Liu, B., et al. 2019, Nature, 569, 378

Ling, Z., Qiao, L., Liu, C., et al. 2019, Planetary and Space science, 179, 104741

Ling, Z. C., Jolliff, B. L., Liu, C. Q., et al. 2018, 49th Lunar and Planetary Science Conference 2018, `https://www.hou.usra.edu/meetings/lpsc2018/pdf/1939.pdf`

Lucey, P. G., Taylor, G. J., Hawke, B. R., & Spudis, P. D. 1998, Journal of Geophysical Research: Planets, 103, 3701

McGetchin, T. R., Settle, M., & Head, J. W. 1973, Earth and Planetary Science Letters, 20, 226

McKay, D. S., Heiken, G., Basu, A., et al. 1991, in Lunar Sourcebook, eds., G.H. Heiken, D. Vaniman, & B. French (Cambridge: Cambridge Univ. press), 285

Melosh, H. J. 1989, Impact cratering: A Geologic Process, 11 (Oxford Univ. Press)

Moriarty III, D. P., & Pieters, C. M. 2018, Journal of Geophysical Research: Planets, 123, 729

Morrison, D. A. 1998, in Lunar and Planetary Science Conference, 29, 1657

Nelson, D. M., Koeber, S. D., Daud, K., et al. 2014, in Lunar and Planetary Science Conference, 45, 2861

Oberbeck, V. R. 1975, Reviews of Geophysics, 13, 337

Ostrach, L. R., Robinson, M. S., Denevi, B. W., & Thomas, P. C. 2011, in Lunar and Planetary Science Conference, 42, 1202

Pasckert, J. H., Hiesinger, H., & van der Bogert, C. H. 2018, Icarus, 299, 538

Petro, N. E., & Pieters, C. M. 2004, Journal of Geophysical Research: Planets, 109, E06004

Petro, N. E., & Pieters, C. M. 2008, Meteoritics & Planetary Science, 43, 1517

Pieters, C. M., Tompkins, S., Head, J. W., & Hess, P. C. 1997, Geophysical Research Letters, 24, 1903

Pike, R. J. 1974, Earth and Planetary Science Letters, 23, 265

Qiao, L., Ling, Z., & Fu, X. 2019, Icarus, 333, 37

Quaide, W. L., & Oberbeck, V. R. 1968, Journal of Geophysical Research, 73, 5247

Robinson, M. S., Brylow, S. M., Tschimmel, M., et al. 2010, Space Science Reviews, 150, 81

Salisbury, J. W., Adler, J. E. M., Smalley, V. G., & Ring, J. 1968, MNRAS, 138, 245

Sharpton, V. L. 2014, Journal of Geophysical Research: Planets, 119, 154

Shearer, C. K., Jolliff, B. L., Alkalai, L., et al. 2011, in Solar System Sample Return Missions, 1611, 5018

Stuart-Alexander, D. E. 1978, Geologic Map of the Central Far Side of the Moon (United States Geological Survey)

Vaughan, W. M., & Head, J. W. 2014, Planetary and Space Science, 91, 101

Whitten, J., & Head, J. W. 2015, Planetary and Space Science, 106, 67

Wilhelms, D. E., Howard, K. A., & Wilshire, H. G. 1979, Geologic Map of the South Side of the Moon (United States Geological Survey)

Wilhelms, D. E., John, F., & Trask, N. J. 1987, The Geologic History of the Moon (USGS Professional Paper)

Xie, M., & Zhu, M.-H. 2016, Earth and Planetary Science Letters, 440, 71

Yingst, R. A., Chuang, F. C., Berman, D. C., & Mest, S. C. 2017, in Lunar and Planetary Science Conference, 48, 1680

Zhu, M.-H., Wunnemann, K., & Potter, R. W. K. 2015, Journal of Geophysical Research: Planets, 120, 2118